Bacterial cellulose/graphene oxide aerogels with enhanced dimensional and thermal stability

Susana C. Pinto[1], Gil Gonçalves*[1], Stefania Sandoval[2], Ana M. López-Periago[2], Alejandro Borras[2], Concepción Domingo[2], Gerard Tobias[2], Isabel Duarte[1], Romeu Vicente[3] and P.A.A.P. Marques*[1]

[1]TEMA, Mechanical Engineering Department, University of Aveiro, P-3810-193 Aveiro, Portugal

[2]Institut de Ciencia de Materiales de Barcelona (ICMAB-CSIC), Campus UAB, 08193, Bellaterra, Spain

[3]RISCO, Civil Engineering Department, University of Aveiro, P-3810-193 Aveiro, Portugal

*Corresponding authors. E-mail: ggoncalves@ua.pt (Gil Gonçalves) and paulam@ua.pt (Paula Marques)

Highlights:

- Bacterial cellulose/graphene oxide (BC/GO) aerogels were prepared by solvent mixing
- A small amount of DMSO addition during hydrogel formation allow pores orientation
- BC/GO reduced with NH3 (gas-phase) show enhanced mechanical and thermal performance
- The reduced BC/GO aerogels present notable values of electric conductivity

Abstract

We present a novel method for processing bacterial cellulose/graphene oxide (BC/GO) aerogels with multifunctional properties. The addition of a small amount of dimethyl sulfoxide (DMSO) to the aqueous dispersion of the nanomaterials during the gelification process affected the water freezing temperature of the system and thereby affecting the porous structure of the aerogel obtained after liophilization. The possibility to obtain small and elongated pore with axial orientation allowed a significant improvement of the structural stability of the aerogels. Moreover, the aerogels reduction by thermal treatment with ammonia gas induced crosslinking between the different nanophases, thus given an incremental factor for the mechanical performance of the aerogels under harsh conditions. The resulting aerogels also showed significant improvements in terms of thermal stability and electrical conductivity. These multifunctional BC/GO aerogels present high potential as

sustainable and ecological alternative materials for lightweight packaging, filters for atmosphere and water treatment, or energy applications.

Keywords: bacterial cellulose; graphene oxide; reduction treatments; dimensional stability; thermal stability

1. Introduction

Cellulose is the most abundant biopolymer in earth, with an annual production of about 1.5 trillion tons, mostly for paper and textile industries (Du, Zhang, Liu, & Deng, 2017). Indeed, humans have been exploring cellulose since ancient times due to its high availability (e.g. cotton, wood, hemp) and easy processability for daily routine materials (Klemm, Heublein, Fink, & Bohn, 2005). Recently, nanotechnology is having a major impact on the development of several new approaches for processing cellulose (bacterial or vegetal). Nanocellulose arises as one of the most sustainable nanomaterial due to its high availability, biodegradability and biocompatibility, with promising applications in areas of environmental remediation, medical care, cosmetics and beyond (Wang, Urbas, & Li, 2018). This nanomaterial has been intensely explored for the development of multifunctional bio-based nanomaterials with several different architectures, including highly porous aerogels and mechanically strong paper or films (Laromaine et al., 2018) (Lavoine & Bergstrom, 2017).

Beside the potential applications of nanocellulose by itself, the incorporation of an additional nanophase can provide the appearance/improvement of outstanding properties due to the establishment of synergistic effects (Lavoine & Bergstrom, 2017)(Vilela et al., 2018). The application range of nanocellulose-based nanocomposites has thus been extended to the fields of antibacterial materials, sensors, catalysis and energy (Alonso-Díaz et al., 2019) (H. Wei, Rodriguez, Renneckar, & Vikesland, 2014).

Recently, graphene oxide (GO) outstands as one of the most appealing nanomaterial for applications in environmental science, energy storage, and medical science (Z. Li, Wang, Li, Feng, & Feng, 2019). Moreover, it has been widely explored as a reinforcing agent for cellulose macrostructures for the development of multifunctional materials (Zhou et al., 2019). GO nanosheets are graphene derivatives decorated with several oxygenated functional groups (carboxylic, hydroxyl and epoxy) on their basal planes and edges, resulting in a hybrid carbon nanostructure comprising a mixture of sp2 and sp3 domains (Bianco et al., 2013) (Dreyer, Park, Bielawski, & Ruoff, 2010). Concerning the compatibility between cellulose and GO, it is reported that the highly oxygenated GO interacts with cellulose hydroxyl groups by the establishment of hydrogen bonds (Song et al., 2016) (Song et al., 2017) resulting in the formation of mechanical stable nanocomposites (X. Wei et al., 2019) with an effective 3D interconnected network (Jiang, Cui, Song, Shi, & Ding, 2018). Many studies give insights about the fabrication of cellulose/GO nanocomposite structures for several applications, e.g., to remove heavy metals, organic dyes, oils or pesticide residues from fluids and for adsorption of air pollutants (X. Wei et al., 2017) (Mi et al., 2018), (Yao et al., 2017a), (Xiong Chen, Zhou, Zhang, You, & Xu, 2016), (Yakout, El-Sokkary, Shreadah, & Abdel Hamid, 2017) (H. Luo et al., 2018); in energy devices, such as supercapacitors (Wan, Jiao, & Li, 2017) (Zheng, Cai, Ma, & Gong, 2015), (Y. Zhang et al., 2017), in electro-magnetic interference shielding field (Wan & Li, 2016), and for biomedical applications with particular relevance in the field of tissue

2

engineering (Ramani & Sastry, 2014) (Ege, Kamali, & Boccaccini, 2017) (Shao, Liu, Liu, Wang, & Zhang, 2015).

The inherent interfacial compatibility of polar nanocellulose with GO provides a stimulating starting point to explore solution-based methodologies for the preparation of homogenous dispersions, in which the structural integrity of the biopolymer matrix is improved. Innovative ways should be developed to maximize the interactions between the matrix and filler, since this is the dominant and key factor in the enhancement of the specific surface area and mechanical performance. For example, the abundant oxygen containing groups in GO likely interact with the hydroxyl groups in cellulose through hydrogen bonds. This has been proven by Yao et al. (2017) by using ultrasonic treatment for composites preparation, in which the high energy supply of ultrasounds induced fast formation of hydrogen bonds. However, the ultrasound method is not the most adequate to prepare three-dimensional structures, since cavitation can easily break the delicate gel framework. The most popular fabrication methods of cellulose/GO in the form of aerogels/foams include freeze-casting, supercritical fluids (ethanol or carbon dioxide) and Pickering (Lavoine & Bergstrom, 2017), (Martoïa, Cochereau, Dumont, Orgéas, & Terrien, n.d.), (Borrás et al., 2018). Particularly, the directional freeze-casting method could create hierarchical materials with aligned porous structures and high mechanical robustness (Mi et al., 2018) (Wicklein et al., 2014). Importantly, this synthetic methodology offers a high control over the pore size and density of nanocellulose-based nanocomposites.

The establishment of chemical crosslinking between nanocellulose and GO is another important strategy explored for the improvement of the dimensional stability of nanocomposite foams. Wicklein et al. (Wicklein et al., 2014) developed ultralight and anisotropic porous foams of cellulose nanofibers with GO by studying the combination of a crosslinking agent (boric acid) addition and directional freeze-casting. The foams revealed excellent combustion resistance, thermal conductivity and high radial mechanical resistance (even after exposure to 85 % rh). Recently, Ge et al. (Ge et al., 2018) reported the development of an ultra-strong aerogel, based on carboxymethyl cellulose and GO crosslinked also resourcing/using boric acid. This composite material produced attained fairly good compressive strength and Young modulus of 349 and 1029 kPa, respectively compatible with different applications. Other examples reporting the covalent linkage between nanocellulose and GO for the formation of macrostructures with improved properties can be easily found in the literature (Y. Liu, Zhou, Zhu, et al., 2015). However, this strategy has some clear limitations, including restrained stability, complex surface chemistry, restrictions for geometrical confinement, the use of organic solvents and the need of purification of the final materials.

A simple way to improve the dimensional and mechanical stability of lightweight and hydrophilic GO based materials, especially in wet environments, consists on GO reduction, thus removing oxygen containing functional groups and, consequently, decreasing its original hydrophilicity (Wen, Wu, Zhang, Li, & Shi, 2017)(Xiong et al., 2018). Besides, the tailoring of GO surface chemistry by reduction could help to increase its reactivity for amphiphilicity-driven assembly strategy. Recently, Xiong et al. (Xiong et al., 2018) reported an efficient approach for constructing hybrid materials based on a net of 1D cellulose nanofibers wrapped in GO nanosheets. Their findings showed that the interface-driven assembly between the two components is mainly governed by the level of reduction of GO nanosheets, where highly reduced GO are tightly surrounded by a dense conformal nanocellulose network (Xiong et al., 2018). Therefore, the morphology and dimensional stability of 3D bacterial cellulose/ graphene

3

oxide (BC/GO) aerogels can be tailor-made by exploring different reduction strategies for improved interfacial hydrophobic-hydrophilic interactions between the individual nanoelements.

This work can represent an important step forward to the development of novel multifunctional BC-based aerogels reinforced with GO for improved performance in different environments, envisaging lightweight structures for packaging, filters for atmosphere and water treatment, or energy applications. Taking these considerations into account, in this study, it is presented a simple, fast, and environmentally friendly preparation method of BC/GO aerogels with different ratios, e.g., 90/10, 75/25 and 50/50. Herein, special focus was directed towards the effect of the addition of a residual amount of dimethyl sulfoxide (DMSO) to the BC/GO aqueous suspension on the structure of the resulting aerogels. Moreover, the impact of two different types of reduction treatments applied to the aerogels, either with an aqueous solution of hydrazine (N2H4) or with ammonia (NH3) gas, in their chemical and structural features was studied.

2. Experimental

2.1. Synthesis of BC/GO aerogels

Bacterial cellulose (BC) aqueous suspension nano-fibrils with 1 % of solids was used as the cellulose source in this work (kindly supplied by BCTECHNOLOGIES, Lda.). BC and GO (Graphenea® in aqueous suspension of 4 mg/mL) were thoroughly mixed for 1 h at room temperature (RT). Four BC/GO sample compositions were prepared (100, 90, 75 and 50 wt. % of BC with respect to the GO dry mass), which are designated hereafter by BC, BC/GO10, BC/GO25 and BC/GO50, respectively. The composites were prepared by directly mixing both suspensions under vigorous stirring with and without the addition of DMSO (1.0 μL and 2.5 μL DMSO:100 μL of aqueous suspension) during the mixture. The final blends were placed in a cylindrical mould, frozen at -20 ºC and freeze-dried in a LyoQuest-Telstar freeze dryer. The samples prepared with 1.0 μL of DMSO were reduced using two different approaches, which involve liquid and gas phase reduction of the material in presence of (N2H4) (Girão et al., 2016) or NH3 (Sandoval et al., 2016). In the first case, the aerogels were immersed into a (N2H4) solution (1μL/mL) at RT for 24h. Then, the aerogels were thoroughly washed with distilled water and dried again by lyophilisation. The second approach consisted in annealing the sample at 220 ºC under a continuous flow of NH3 gas. The samples processed with NH3 were then purified by vacuum treatment to remove the residual NH3 adsorbed on the aerogel. In both cases, treatments might lead to the N-functionalization/doping of the graphene derivative (Sandoval et al., 2016). A scheme of the employed methodology is shown in Figure 1.

2.2. Characterization

The morphology of the samples was characterized using an ultra-high-resolution analytical scanning electron microscope HR-FESEM Hitachi SU-70 operating at an accelerating voltage of 15 kV. The samples (cylinders of 12 mm in diameter and 10 mm in height) and densities (23 kg/m3) were analysed in a micro-computed tomography (μCT) equipment from SkyScan 1275 (Bruker μCT, Belgium) with penetrative X-rays of 20 kV and 175 μA, in a high resolution mode with a pixel size of 10 μm and 450 ms of exposure time. NRecon and CTVox softwares were used for 3D-reconstruction and CTan software was used in morphometric analysis. A representative reduced volume of interest (VOI) was defined in both samples with a volume of 500 mm3 in 3D reconstruction and morphometric analysis (pore size distribution). The

4

chemical composition of the foams was analysed by Fourier Transform Infrared Spectroscopy - Attenuated Total Reflectance (FT-IR-ATR) (Bruker Tensor 27) spectrophotometer between 4000 and 400 cm-1, with a resolution of 4 cm-1 and 64 scans. XPS spectra were acquired in an Ultra High Vacuum (UHV) system equipped with a hemispherical electron energy analyser (SPECS Phoibos 150), a delay-line detector and a monochromatic AlKα (1486.74 eV) X-ray source. High resolution spectra were recorded at normal emission take-off angle and with a pass-energy of 20 eV. The thermal stability of the composites aerogels was assessed by a thermogravimetric analyser (Netsch, Jupiter STA 449 F3) at a scanning rate of 10 ºC/min, in the temperature range of 30–800 ºC, under an oxidative atmosphere (synthetic air). For the swelling tests, the dry specimens were allowed to hydrate in excess distilled water at RT. The weights of the hydrated samples were measured at timed intervals, following removal of excess water by gentle blotting. The swelling ratio (Q) was determined using Equation 1, where Wi is the weight of the swollen material at time i and W0 is the weight of the dried foam.

$$Q = \frac{(W_i - W_0)}{W_0} \qquad \text{(Eq. 1)}$$

Contact angle measurements were carried out with OCA 20 from Dataphysics. The measurements were performed at RT using the sessile drop method and the Laplace-Young fitting. Uniaxial compression tests and dynamic cyclic compression tests were performed using Microservo Magnetic Tester equipment (MMT-101N; manufactured by Shimadzu Corporation, Japan) equipped with a 100 N load cell. The tests were carried out for 5 % deformation, at a frequency of 0.3 Hz for 1,000 cycles and quasi-static compression at a cross-head speed of 1.0 mm/min.

3. Results and discussion

3.1. Effect of solvent composition on BC/GO aerogels

The BC/GO aerogels were prepared by vigorous stirring of mixtures of the aqueous suspensions of both individual components. In this process, BC nanofibers were dispersed and self-assembled on the surface of GO (Y. Liu, Zhou, Tang, & Tang, 2015). The synthesis of a BC/GO aerogel is schematically illustrated in Figure 1. The SEM observation of the as-prepared BC/GO aerogels without DMSO addition confirms the porous structure and the homogenous mixture between the cellulose fibrils and the GO sheets, being difficult to distinguish both components (Figure 1). The chemical composition of both phases allows for the establishment of strong hydrophilic interactions (Yang et al., 2017) and hydrogen bonds (Fang, Zhou, Deng, Zheng, & Liu, 2016), thus endorsing strong entanglement that leads to the formation of 3D networks. Independently of the BC/GO ratio used, the aerogels exhibited an interconnected porous structure, with distribution of pore size width in the range from a few microns to hundreds of micrometers.

As mentioned, this work first explores the possibility to induce structural features of BC/GO aerogels by the DMSO addition to aqueous BC/GO suspensions during the processing of the samples. Hence, the effect of adding a small amount of DMSO to the BC/GO aqueous mixture (1.0 and 2.5 µL DMSO / 100 µL aqueous mixture) was studied. Despite the very low volumetric fraction of DMSO added, the structural changes observed on the BC/GO aerogels were remarkably (Figure S1, SI). We observed that with DMSO concentration increase (0, 1.0 and 2.5 µL), more compact structures were formed. Indeed, the samples prepared with 2.5 µL presented a collapsed porous structure closer to a film-like structure. Therefore, after these results our studies were focused with samples obtained without and with 1.0 µL of DMSO.

SEM micrographs of the BC/GO aerogels with 1.0 µL of DMSO showed that the final pore size and morphology of the later was significantly changed. In fact, in the absence of DMSO, the aerogel presents a more homogeneous porosity with round shaped pores (Figure 1). While, in the presence of DMSO, a preferential formation of small and elongated pores, with axial orientation was observed. Recently, the design of artificial interfaces has been reported by exploring the limits of GO gelation by microphase separation in water-miscible isopropanol. The low intercalation energy of water promotes the formation of an artificial liquid interface with high local concentration of GO, which after solvothermal treatment can be assembled into interconnected frameworks (C. Luo et al., 2019). DMSO is a polar solvent with a freezing point of 18 °C, (Ozmen, Dinu, & Okay, 2008) (Wong et al., 2012) having capacity to accept hydrogen bonds. DMSO/water mixtures exhibit a marked freezing point depression due to the formation of stable DMSO/water complexes. For instance, it has been reported that by adding DMSO to water at a volume ratio of 1:1, the freezing point of the resulting mixture is lowered to - 52 °C (Ozmen et al., 2008) (Mattiasson, Kumar, & Galeaev, 2009).

To further investigate the different structural features of the BC/GO aerogels produced in the presence of DMSO, µCT measurements were conducted. The 3D reconstruction provides information related with the pore structure and interconnectivity as well as pore wall thickness. 3D reconstructions from µCT for BC/GO aerogels with DMSO are shown in Figure 2. The images suggest interconnected porous structures composed mostly by open-cell pores (highly open porosity with values above 90 %). The µCT reveals that the increase of the GO concentration in the aerogels promotes thicker pore walls formation, specially from 10 to 25 % of GO. Additionally, BC/GO50 showed lower pore size distribution. From Ctan software, the pore volume distribution was determined (Figure S2, SI). The µCT results are in accordance with SEM analysis, showing that the BC/GO50 has a narrower pore size distribution, with 75 % of the pore size below 200 µm, than BC/GO25 and BC/GO10, with around 60 %.

When the suspension of BC/GO is frozen, the growth of ice crystals tends to accumulate the nanomaterials between their boundaries (Yao et al., 2017a). The increase of GO with respect to BC fibrils appears to allow its self-assembly on the ice crystal borders endorsing thicker pore walls resulting in the establishment of stable aerogel structure. This justifies the fragile nature of the BC/GO aerogel, which has been abandoned for further studies.

3.2. Effect of reduction treatment on BC/GO aerogels

In the previous section, it was reported the structural anisotropy of the BC/GO foams induced by simple solvent mixing during the processing of the samples. The visual inspection of the BC/GO aerogels clearly evidenced the effectiveness of the GO reduction process in both cases by presenting its characteristic final black colour (Figure 1). It is important to notice that the reduction treatments applied to the aerogels do not appear to significantly affect the porous structure. Although the treatment with NH3 gas seems to be more conservative than the solution treatment with N2H4, the collapse of the structure in the latter was not observed (Figure S3, SI).

XPS analysis was conducted in order to assess the surface composition of the different aerogels. Table 1 gathers the elemental composition of each aerogel as well as the O/C and N/C ratios.

Analysis of the non-reduced specimens shows a high at. % for the carbon (C1s) and oxygen (O1s), which corresponds to the main elements on the starting nanomaterials. After reduction via N2H4 solution or thermal treatment with NH3 gas, the at. % of the O1s was significantly

6

reduced. The calculation of the O/C ratio provides an indirect estimation of the extent of reduction. It was observed that the treatment with NH3 (O/C ~ 0.20) is much more effective on the reduction process of GO than processing with N2H4 (O/C ~ 0.32), having into consideration the reference value of non-treated samples (O/C ~ 0.42 – 0.50). It is important to mention that the reduction efficiency of the aerogels is mainly governed by the effect of the treatment(s) on GO nanophase. XPS studies performed with reduced BC aerogels with NH3 revealed a similar oxygen contents to that non-treated BC aerogels (37 at. %, Figure S4, SI).

A significant N-loading of the BC/rGO25 aerogels occurred when the reduction process via NH3 treatment was employed, with ca. 8.3 at. % of N. However, it was observed that the at. % of N determined in the BC/GO50 aerogels was only of 1.1 at. % of N. The higher N content in the aerogels with less GO percentage suggests that the N-loading occurred preferably in the cellulose backbone by the formation of amine, amide, imide and lactam groups (Cagniant et al., 2002; W. Luo et al., 2014; Pertile, Andrade, Alves, & Gama, 2010). Yet, control experiment of reductive thermal treatment of pristine BC foams, under the same experimental conditions, revealed a total concentration of N lower than 1 at. %. Hence, N must be introduced in the BC/GO aerogel mainly cross-linked at the interface of GO and BC nanostructures (as verified by XPS and FTIR), instead of modifying the GO graphitic structure or BC backbone separately (Figure 3). Importantly, the results revealed that the crosslinking process is much more efficient for the sample BC/rGO25NH3 due to a high intensity of the signal N1s at 400 eV, which corresponds to binding energies of N moieties (Figure 3 (a)). These results can be attributed to the high miscibility of the nanophases at the ratio 75/25, which facilitates gelification under equilibrium. The saturation with the nanophases is observed at the ratio 50/50 with the appearance of small aggregates verified during gel formation.

The XPS spectrum of N1s with peak fitting for BC/rGO25NH3 sample is shown in Figure S5, SI. The N1s peak can be deconvoluted into three main components, which are usually assigned to graphitic N (quaternary species, N+ 401.5 eV), pyrrolic N (400.03 eV) and pyridinic N (398.64 eV) groups (Ma et al., 2016). However, both pyrrolic N and pyridinic N signals overlap with the binding energies corresponding to aliphatic moieties, namely amine and amide groups respectively (Sandoval et al., 2016). The presence of amide groups clearly indicates the possible establishment of chemical crosslinking between the nanophases of the aerogel materials. However, the formation of structural moieties due to the substitution of C atoms from the skeleton of both BC and GO cannot be discarded. The mechanism for the establishment of covalent bonds is not clear; however, it is anticipated here, that in case of amide groups, it can preferentially occur between the free carboxylic groups on GO, and free amine groups on BC generated during the thermal reduction (Figure S5, SI).

FT-IR spectra analysis of BC/GO25 (Figure 3 (d)) reveal the presence of abundant hydrophilic oxygen containing groups, including C=O (1732 cm−1), C-O (1160 cm−1, 1110 cm−1, and 1060 cm−1), and O-H (1625 cm−1 bending and 3350 cm−1 stretching). The peaks around 2850-2950 cm−1 and 1310-1370 cm−1 are attributed to C–H vibrations (Shao et al., 2015) (C. Li, Wu, Liang, Chen, & Yu, 2017). After reduction with NH3 or N2H4, the peaks ascribed to the oxygen functionalities suffer a significant decrease of intensity (Tao et al., 2017) (Bang et al., 2018). Moreover, the reduction process also promotes the appearance of new bands originated by the incorporation of N-based functionalities into the aerogels. For instance, the peaks located at 1230 cm-1, 1558 cm-1 and 1655 cm-1 can be ascribed to C-N and C=C and C=N, respectively. The band corresponding to N–H vibrations around 3200 cm−1 is probably overlapped with the O–H bond vibrations. Importantly, it was observed the appearance of the new band at 1430

7

cm-1 for the sample thermally treated with NH3 (Saska et al., 2012), which can be assigned to the formation of amide groups resultant from the crosslinking between BC and GO which is in accordance with XPS analysis.

3.3. Dimensional stability of the BC/GO foams

Uniaxial compression tests were performed up to 80 % of deformation and stress–strain curves are shown in Figure 4 (a). For BC/GO25 and BC/rGO25NH3 a typical cellular behaviour under compression loading (Duarte, Vesenjak, Krstulović-Opara, & Ren, 2018) were obtained (as represented in Figure S6, SI). First, an initial well-defined elastic stage was observed (up to 12 %), where stress changes linearly with strain, followed by plastic region in which, the materials undergo irreversible deformation (10-55 %). This region is designated by the Stress Plateau and is characterized by low stress variation with continuous deformation due to the skeleton structure collapse. Then, when the cell walls come in contact with each other, densification occurs (the stress increases abruptly). Through the compression, no cracks were observed, and the aerogels became dense and tough, with small or negligible lateral expansion. For BC/GO25 without DMSO specimen, the transition from linear to non-linear stress–strain behaviour is not clear, the initial region of linear elasticity merges itself with the long collapse zone described as the Plateau step, in which the variation of the stress is low. Some important parameters were determined from stress/strain curves, compressive strength (CS) at 40 % of deformation and Young's modulus. The CS (at 40 % of strain) and YM (determined by the slope in the linear region) of BC/GO25 without DMSO, BC/GO25, BC/rGO25NH3 and BC/rGO25N2H4 are shown in Figure 4 (b).

With the addition of DMSO, there is alignment in the axial porosity and therefore high YM and CS at 40 % of deformation were observed. The CS and YM of the BC/GO25 aerogel at 40 % strain of were 20 kPa and 80 kPa respectively, which were 120 and 200 % higher than that of the BC/GO25 aerogel without DMSO. The BC/rGO25NH3 specimen presents high stress values in the Plateau region (high load bearing capacity) and also high YM (300 % and 35 % higher than BC/GO25 without DMSO and BC/GO25, respectively). This improved performance is attributed to the crosslinking promoted by the reduction with NH3 gas, thereby enhancing the skeleton structure of aerogel. These results are in agreement with those obtained for cyclic tests (Figure 4 (c), with the BC/rGO25NH3 having the best mechanical performance at low deformations. The YM values obtained are quite lower to those obtained by Ge et al. for ultra-strong aerogel based on carboxymethyl cellulose and GO crosslinking mediated by boric acid (YM values ranging from 228 KPa to 1 MPa for aerogels with 25 kg/m3 of density) (Ge et al., 2018), although higher to those obtained by Zhang et al (X. Zhang, Liu, Duan, Jiang, & Zhang, 2017) that prepared ultralight graphene/cellulose nanocrystal (CNC) hybrid aerogels and with values of YM (20-60 kPa).

The mechanical integrity of BC/GO foams under harsh conditions is a crucial factor to explore their potential applications. For this reason, the mechanical behaviour under dynamic cyclic compression was studied in different environments (dry and wet conditions). A strain amplitude of 5 % was selected, which was verified to be in the linear regime. After the dry dynamic cyclic compression tests, the specimens did not present significant structural changes as they recover its original shape with no mechanical failure. Besides, after a first period of accommodation, the materials present a quasi-constant value of stress amplitude. Figure 4 (c) illustrates the stress amplitude for 1,000 cycles. In a dry environment, the stress amplitude of the aerogels increases on the following order: starting with the lower value for the aerogel resultant from the simple mixture BC/GO (2.6 kPa) to the aerogel formed with addition of

8

DMSO (3.8 kPa) and to the aerogel resultant from the thermal reduction with NH3 (5.4 kPa). It is important to notice the impressive improvement of stress amplitude of 110 % for aerogel BC/rGO25NH3. This value results from the structural synergistic effects from the synthetic process, in which the addition of DMSO to the gel mixture control the formation of axial porosity and extend crosslinking in the aerogel thermally treated with NH3. Besides, it is important to notice that for aerogels BC/rGO50NH3 a lower value of stress amplitude of 4.5 kPa was observed, which can be explained by the lower extent of crosslinking (XPS), the presence of structural defects through the formation of agglomerates of the individual components, and the non-homogeneous mixture of the nanophases of the aerogel. Contrarily, in a wet environment, the non-reduced foams easy lose their shape during the compression tests, while the reduced forms undergo the loading/unloading process without significant dimensional changes. Overall, the mechanical response in dry conditions is superior to wet conditions due to the phenomena of diffusion, and structure collapse promoted by water swelling. Despite the adverse conditions, the aerogels BC/rGO25NH3 reveal a highest resilience by presenting a stress amplitude of 3.5 kPa, that correspond to an increase of 1300 % compared to the BC/GO25 aerogel (Figure 4 (c) and Figure 4 (d)).

The dimensional water stability of the produced aerogels was further studied by assessing the hydrophobic/hydrophilic nature of the aerogels, swelling (Figure 5 (a)) and water contact angle determination (Figure 5 (b) and Figure 5 (c)). Figure 5 (a) shows the swelling kinetics of the foams under study, which clearly indicates a distinct behaviour between the as-prepared foams and the foams subjected to a reduction process. The non-reduced composites present an initially high swelling ratio (Q), followed by a gradual decrease in absorption with time indicating water loss, reaching the equilibrium stage after approximately 3 h. For the reduced composites, the opposite profile was observed, i.e., the swelling gradually increases until the equilibrium after 4 h, reaching lower Q values than the previous series. The same tendency was verified by Girão et al. (Girão et al., 2016) for collagen/graphene oxide scaffolds. For the non-reduced foams, the swelling behaviour is higher for the BC/GO50 than for the BC/GO25 series, most probably due to a structure collapse that closes the pores. After reduction, the dimensional stability of the aerogels improves significantly. However, the reduction of the aerogels with NH3 at 220 ºC seems to be more effective comparatively to N2H4 reduction (as observed by XPS), due to the smaller swelling values. These results suggest that the thermal reduction with NH3 increases the density of hydrophobic domains at the interface of the aerogel that limits the water flow into the pores.

The highly porous and hydrophilic surface of the BC/GO materials was revealed by water contact angle (WCA) measurements, where the water droplet was quickly absorbed on their surface, making not possible the measurement of associated WCA. This result is in agreement with the swelling tests where the BC/GO aerogels collapse fast when exposed to water solutions. Also, an immediate spread of the water droplet was observed after water drop contact with the sample reduced with N2H4 (Figure 5 (b)). These results can be understood by the contribution of two main factors: the oxygen-based functional groups still present at the surface of rGO, and the partial collapse of the interfacial porosity of the BC/GO aerogels during the N2H4 treatment in aqueous solution. The N2H4 reduction approach can be considered less effective to the aerogel, since the water flow partially degrades the structural porosity at the interface. Only the specimens reduced with NH3 present high hydrophobic character with WCA values that reach ca. 120 degrees (Figure 5 (c)). These results indicate a higher

effectiveness of the reduction treatment with NH3 vs. N2H4 for the final dimensional water stability of the BC/GO aerogels, by promoting an extended reduction of GO on the aerogel and simultaneously preserving the structural porosity.

3.4. Thermal stability

TGA measurements were carried out to investigate the thermal stability of the several BC/GO specimens prepared in this study. The TG curves in oxidative atmosphere of individual components (BC and GO) and BC/GO25 aerogel series are shown in Figure 6 (a). Thermogravimetric curves indicate that at ca. 400 ºC, the BC/GO25 had a weight loss of 50 wt. % while BC lost up to 90 % of its initial weight. The enhanced thermal stability of the BC/GO25 aerogel comparatively to pure BC may be attributed to the interaction between BC and GO, forming an aerogel network cross-linked and restricting the movement of the polymer chains at the interface of the BC and GO, and also to the formation of a char layer that creates an indirect pathway for volatiles. The weight loss observed up to ca. 120 ºC corresponds to the evaporation of absorbed water. BC, GO and BC/GO25 nanocomposites present two weight loss stages. GO has two severe weightlessness stages: the weight loss, between 150-200 °C, mainly assigned to the loss of oxygen functional groups of GO and between 450 ºC and 520 ºC attributed to the reaction of the more stable carbonaceous residue in presence of the oxidizing atmosphere (calcination of the conjugated carbon skeleton of GO). In the case of BC, the first stage located between 260 ºC and 310 ºC is assigned to the depolymerisation of BC, while the subsequent second stage situated between 310 ºC and 435 ºC for BC/GO25 corresponds to the generation of CO, CO2 and H2O (Ren et al., 2018) (Gan, Zakaria, Chia, & Kaco, 2018) (Yao et al., 2017b) (Xiaofang Chen et al., 2019). The reduced forms of BC/GO aerogels present a later degradation. The main decomposition onset is slightly shifted to higher temperatures compared to the non-reduced forms, suggesting the positive effect of the reduction process on the thermal stability. It is believed that this improvement is due to the decrease in the amount of oxygenated functional groups, which improved the ability of aerogels to tolerate high temperatures in the oxidative atmosphere (Cheng et al., 2017). The temperature of combustion can be also correlated to the presence of N-containing fractions within the aerogel network that, as previously reported, confer enhanced thermal stability against oxidation when these species are introduced within a graphitic network (Sandoval et al., 2014). The TGA results showed that the reduction of aerogels with N2H4 and NH3 was not fully completed, because there is a slight weight loss that occurred over the temperature range of 160–260 °C. This thermal event can be ascribed, not only to the loss of the remaining oxygen functional groups, but also to the elimination of N-containing aliphatic moieties, which presence has been confirmed by XPS and that occurs simultaneously during the reduction step.

All the specimens were tested to evaluate the burning behaviour when a flame of an ethanol lamp is applied to the samples for three seconds. For BC/GO25 aerogels, as well as their reduced forms, the flame extinguished instantaneously, and the specimens maintained their shape during burning without dripping or smoke release (Figure 6 (b)). These results suggest that these porous materials have flame-retardant properties. A control test was performed to a BC aerogel and, in this case, the specimen burned completely (Figure 6 (c)). One possible reason for the enhanced thermal stability of BC could be the layered structure of the GO, which tends to form a char layer at the surface, which avoids or makes difficult the release of the volatile degradation products, delaying the degradation of the whole aerogel by offering

indirect pathways for the volatiles release. Also, the flame temperature of an alcohol burner was lower than the combustion temperature of aerogels constituents (Cheng et al., 2017).

3.5. Electrical properties

The electric conductivity was determined from measuring the resistance at different frequencies (Table 2). A little compression was made to ensure good contact between the rGO layers and thus a densely network with good electron transportation was obtained. The BC/GO composites have electrical insulation abilities, 5.9×10^{-07} and 1.8×10^{-06} S/m for BC/GO25 and BC/GO50, respectively, due to the presence of a large number of oxygen-containing functional groups on the surface of GO, and also in BC, which delays the electrons transport. The reduction with NH_3 at 220 ºC is more favourable to produce high BC/rGO conductors when compared to the ones reduced with N_2H_4 (Table 2). After the reduction treatments, a large fraction of the oxygen-containing groups were removed and π- π bonds were restored on the surface of rGO, which facilitates the electrons transportation (Beeran P. T. et al., 2016; F. Liu, Wang, & Tang, 2018; Pottathara et al., 2019; Zhan, Xiong, Yang, Shi, & Yang, 2019). As already mentioned, the increase of the electric conductivity for the specimens reduced with NH_3 is substantially higher, with increments of 12×106 for BC/rGO25NH3 against materials undergoing reduction in presence of N_2H_4 (Table 2). Importantly, it was observed that the significant increase of GO concentration into the BC/GO aerogel composition from 25 % to 50 % does not correspond to a significant improvement of the values of conductivity, after the NH_3 treatment, being these of 7.2×10^{-1} S m^{-1} and 8.7×10^{-1} S m^{-1}, respectively. We can thus infer that there must be a GO concentration threshold that limits the increase of the conductivity of BC/GO aerogels.

From the literature, this is one of the highest values of conductivity ever reported for aerogel architectures composed by a mixture of BC/GO. For example, cellulose nanofibrills films with 3 wt. % UV-reduced GO showed a substantially lower electric conductivity of 6.7×10^{-4} S m^{-1} (Pottathara et al., 2019). Higher values of electric conductivity for similar 3D materials were reported in the literature just in the cases that these were subjected to high temperature treatments (above 500 ºC) and then compressed (Perez-Madrigal, Edo, & Aleman, 2016). These severe treatment conditions promote the thermal decomposition of the nanocomponents promoting graphitization, thus compromising their mechanical integrity.

4. Conclusions

In summary, this work reports a new methodology for the development of multifunctional BC/GO aerogel materials with improved properties. The internal structural morphology of BC/GO aerogels can be easily tuned by the addition of DMSO to aqueous suspensions during the gelification process. The addition of DMSO promotes the formation of small and elongated pores with axial arrangement. Thermal treatment of BC/GO samples with NH_3 revealed to be a less invasive and more efficient treatment for reduction than the use of conventional N_2H_4. Besides, NH_3 thermal treatment promoted the establishment of crosslinking between both nanophases, which enhanced the structural stability. The obtained aerogels showed improved

11

dimensional stability under dry and wet environments, upgraded thermal resistance to oxidation and high electric conductivity (7.2 ×10-1 (S m-1)).

References

Alonso-Díaz, A., Floriach-Clark, J., Fuentes, J., Capellades, M., Coll, N. S., & Laromaine, A. (2019). Enhancing Localized Pesticide Action through Plant Foliage by Silver-Cellulose Hybrid Patches. ACS Biomaterials Science & Engineering, 5(2), 413–419. https://doi.org/10.1021/acsbiomaterials.8b01171

Bang, G. S., Shim, G. W., Shin, G. H., Jung, D. Y., Park, H., Hong, W. G., … Choi, S.-Y. (2018). Pyridinic-N-Doped Graphene Paper from Perforated Graphene Oxide for Efficient Oxygen Reduction. ACS Omega, 3(5), 5522–5530. https://doi.org/10.1021/acsomega.8b00400

Beeran P. T., Y., Bobnar, V., Gorgieva, S., Grohens, Y., Finšgar, M., Thomas, S., & Kokol, V. (2016). Mechanically strong, flexible and thermally stable graphene oxide/nanocellulosic films with enhanced dielectric properties. RSC Advances, 6(54), 49138–49149. https://doi.org/10.1039/C6RA06744A

Bianco, A., Cheng, H. M., Enoki, T., Gogotsi, Y., Hurt, R. H., Koratkar, N., … Zhang, J. (2013). All in the graphene family - A recommended nomenclature for two-dimensional carbon materials. Carbon, 65, 1–6. https://doi.org/10.1016/j.carbon.2013.08.038

Borrás, A., Gonçalves, G., Marbán, G., Sandoval, S., Pinto, S., Marques, P. A. A. P., … Domingo, C. (2018). Preparation and Characterization of Graphene Oxide Aerogels: Exploring the Limits of Supercritical CO 2 Fabrication Methods. Chemistry - A European Journal, 24(59), 15903–15911. https://doi.org/10.1002/chem.201803368

Cagniant, D., Magri, P., Gruber, R., Berlozecki, S., Salbut, P. D., Bimer, J., & Nansé, G. (2002). Ammoxidation of cellulose—a structural study. Journal of Analytical and Applied Pyrolysis, 65(1), 1–23. https://doi.org/https://doi.org/10.1016/S0165-2370(01)00172-3

Chen, Xiaofang, Liang, Y., Wan, L., Xie, Z., Easton, C. D., Bourgeois, L., … Wang, H. (2019). Construction of porous N-doped graphene layer for efficient oxygen reduction reaction. Chemical Engineering Science, 194, 36–44. https://doi.org/https://doi.org/10.1016/j.ces.2018.04.004

Chen, Xiong, Zhou, S., Zhang, L., You, T., & Xu, F. (2016). Adsorption of heavy metals by graphene oxide/cellulose hydrogel prepared from NaOH/urea aqueous solution. Materials, 9(7). https://doi.org/10.3390/MA9070582

Cheng, Y., Zhou, S., Hu, P., Zhao, G., Li, Y., Zhang, X., & Han, W. (2017). Enhanced mechanical, thermal, and electric properties of graphene aerogels via supercritical ethanol drying and high-temperature thermal reduction. Scientific Reports, 7(1), 1439. https://doi.org/10.1038/s41598-017-01601-x

Dreyer, D. R., Park, S., Bielawski, W., & Ruoff, R. S. (2010). The chemistry of graphene oxide. Chem. Soc. Rev., 39, 228–240. https://doi.org/10.1039/b917103g

Du, X., Zhang, Z., Liu, W., & Deng, Y. (2017). Nanocellulose-based conductive materials and their emerging applications in energy devices - A review. Nano Energy, 35, 299–320. https://doi.org/https://doi.org/10.1016/j.nanoen.2017.04.001

Duarte, I., Vesenjak, M., Krstulović-Opara, L., & Ren, Z. (2018). Crush performance of multifunctional hybrid foams based on an aluminium alloy open-cell foam skeleton. Polymer Testing, 67, 246–256. https://doi.org/https://doi.org/10.1016/j.polymertesting.2018.03.009

Ege, D., Kamali, A. R., & Boccaccini, A. R. (2017). Graphene Oxide/Polymer-Based Biomaterials. Advanced Engineering Materials, 19(12), 16–34. https://doi.org/10.1002/adem.201700627

Fang, Q., Zhou, X., Deng, W., Zheng, Z., & Liu, Z. (2016). Freestanding bacterial cellulose-graphene oxide composite membranes with high mechanical strength for selective ion permeation. Scientific Reports, 6, 33185.

Gan, S., Zakaria, S., Chia, C. H., & Kaco, H. (2018). Effect of graphene oxide on thermal stability of aerogel bio-nanocomposite from cellulose-based waste biomass. Cellulose, 25(9), 5099–5112. https://doi.org/10.1007/s10570-018-1946-5

Ge, X., Shan, Y., Wu, L., Mu, X., Peng, H., & Jiang, Y. (2018). High-strength and morphology-controlled aerogel based on carboxymethyl cellulose and graphene oxide. Carbohydrate Polymers, 197, 277–283. https://doi.org/https://doi.org/10.1016/j.carbpol.2018.06.014

Girão, A. F., Gonçalves, G., Bhangra, K. S., Phillips, J. B., Knowles, J., Irurueta, G., … Marques, P. A. A. P. (2016). Electrostatic self-assembled graphene oxide-collagen scaffolds towards a three-dimensional microenvironment for biomimetic applications. RSC Adv, 6(54), 49039–49051. https://doi.org/10.1039/c6ra10213a

Jiang, F., Cui, S., Song, N., Shi, L., & Ding, P. (2018). Hydrogen Bond-Regulated Boron Nitride Network Structures for Improved Thermal Conductive Property of Polyamide-imide Composites. ACS Applied Materials & Interfaces, 10(19), 16812–16821. https://doi.org/10.1021/acsami.8b03522

Klemm, D., Heublein, B., Fink, H.-P., & Bohn, A. (2005). Cellulose: Fascinating Biopolymer and Sustainable Raw Material. Angewandte Chemie International Edition, 44(22), 3358–3393. https://doi.org/10.1002/anie.200460587

Laromaine, A., Tronser, T., Pini, I., Parets, S., Levkin, P. A., & Roig, A. (2018). Free-standing three-dimensional hollow bacterial cellulose structures with controlled geometry via patterned superhydrophobic–hydrophilic surfaces. Soft Matter, 14(19), 3955–3962. https://doi.org/10.1039/C8SM00112J

Lavoine, N., & Bergstrom, L. (2017). Nanocellulose-based foams and aerogels: processing, properties, and applications. J. Mater. Chem. A, 5(31), 16105–16117. https://doi.org/10.1039/C7TA02807E

Li, C., Wu, Z.-Y., Liang, H.-W., Chen, J.-F., & Yu, S.-H. (2017). Ultralight Multifunctional Carbon-Based Aerogels by Combining Graphene Oxide and Bacterial Cellulose. Small, 13(25), 1700453--n/a. https://doi.org/10.1002/smll.201700453

Li, Z., Wang, L., Li, Y., Feng, Y., & Feng, W. (2019). Carbon-based functional nanomaterials: Preparation, properties and applications. Composites Science and Technology, 179, 10–40. https://doi.org/https://doi.org/10.1016/j.compscitech.2019.04.028

Liu, F., Wang, C., & Tang, Q. (2018). Conductivity Maximum in 3D Graphene Foams. Small, 14(32), 1801458. https://doi.org/10.1002/smll.201801458

Liu, Y., Zhou, J., Tang, J., & Tang, W. (2015). Three-Dimensional, Chemically Bonded Polypyrrole/Bacterial Cellulose/Graphene Composites for High-Performance Supercapacitors. Chemistry of Materials. https://doi.org/10.1021/acs.chemmater.5b03060

14

Liu, Y., Zhou, J., Zhu, E., Tang, J., Liu, X., & Tang, W. (2015). Facile synthesis of bacterial cellulose fibres covalently intercalated with graphene oxide by one-step cross-linking for robust supercapacitors. Journal of Materials Chemistry C, 3(5), 1011–1017. https://doi.org/10.1039/C4TC01822B

Luo, C., Lv, W., Qi, C., Zhong, L., Pan, Z.-Z., Li, J., … Yang, Q.-H. (2019). Realizing Ultralow Concentration Gelation of Graphene Oxide with Artificial Interfaces. Advanced Materials, 31(8), 1805075. https://doi.org/10.1002/adma.201805075

Luo, H., Xie, J., Wang, J., Yao, F., Yang, Z., & Wan, Y. (2018). Step-by-step self-assembly of 2D few-layer reduced graphene oxide into 3D architecture of bacterial cellulose for a robust, ultralight, and recyclable all-carbon absorbent. Carbon, 139, 824–832. https://doi.org/https://doi.org/10.1016/j.carbon.2018.07.048

Luo, W., Wang, B., Heron, C. G., Allen, M. J., Morre, J., Maier, C. S., … Ji, X. (2014). Pyrolysis of Cellulose under Ammonia Leads to Nitrogen-Doped Nanoporous Carbon Generated through Methane Formation. Nano Letters, 14(4), 2225–2229. https://doi.org/10.1021/nl500859p

Ma, L., Zhuang, H. L., Wei, S., Hendrickson, K. E., Kim, M. S., Cohn, G., … Archer, L. A. (2016). Enhanced Li–S Batteries Using Amine-Functionalized Carbon Nanotubes in the Cathode. ACS Nano, 10(1), 1050–1059. https://doi.org/10.1021/acsnano.5b06373

Martoïa, F., Cochereau, T., Dumont, P. J. J., Orgéas, L., & Terrien, M. (n.d.). Cellulose Nanofibril Foams : Links between Ice-templating Conditions , Microstructures and Mechanical Properties.

Mattiasson, B., Kumar, A., & Galeaev, I. Y. (2009). Macroporous Polymers: Production Properties and Biotechnological/Biomedical Applications. CRC Press.

Mi, H. Y., Jing, X., Politowicz, A. L., Chen, E., Huang, H. X., & Turng, L. S. (2018). Highly compressible ultra-light anisotropic cellulose/graphene aerogel fabricated by bidirectional freeze drying for selective oil absorption. Carbon, 132, 199–209. https://doi.org/10.1016/j.carbon.2018.02.033

Ozmen, M. M., Dinu, M. V., & Okay, O. (2008). Preparation of macroporous poly(acrylamide) hydrogels in DMSO/water mixture at subzero temperatures. Polymer Bulletin, 60(2), 169–180. https://doi.org/10.1007/s00289-007-0851-0

Perez-Madrigal, M. M., Edo, M. G., & Aleman, C. (2016). Powering the future: application of cellulose-based materials for supercapacitors. Green Chem., 18(22), 5930–5956. https://doi.org/10.1039/C6GC02086K

Pertile, R. A. N., Andrade, F. K., Alves, C., & Gama, M. (2010). Surface modification of bacterial cellulose by nitrogen-containing plasma for improved interaction with cells. Carbohydrate Polymers, 82(3), 692–698. https://doi.org/https://doi.org/10.1016/j.carbpol.2010.05.037

Pottathara, Y. B., Thomas, S., Kalarikkal, N., Griesser, T., Grohens, Y., Bobnar, V., … Kargl, R. (2019). UV-Induced reduction of graphene oxide in cellulose nanofibril composites. New Journal of Chemistry, 43(2), 681–688. https://doi.org/10.1039/C8NJ03563F

Ramani, D., & Sastry, T. P. (2014). Bacterial cellulose-reinforced hydroxyapatite functionalized graphene oxide: A potential osteoinductive composite. Cellulose, 21(5), 3585–3595. https://doi.org/10.1007/s10570-014-0313-4

15

Ren, F., Li, Z., Tan, W.-Z., Liu, X.-H., Sun, Z.-F., Ren, P.-G., & Yan, D.-X. (2018). Facile preparation of 3D regenerated cellulose/graphene oxide composite aerogel with high-efficiency adsorption towards methylene blue. Journal of Colloid and Interface Science, 532, 58–67. https://doi.org/https://doi.org/10.1016/j.jcis.2018.07.101

Sandoval, S., Kumar, N., Oro-Solé, J., Sundaresan, A., Rao, C. N. R., Fuertes, A., & Tobias, G. (2016). Tuning the nature of nitrogen atoms in N-containing reduced graphene oxide. Carbon, 96, 594–602. https://doi.org/https://doi.org/10.1016/j.carbon.2015.09.085

Sandoval, S., Kumar, N., Sundaresan, A., Rao, C. N. R., Fuertes, A., & Tobias, G. (2014). Enhanced Thermal Oxidation Stability of Reduced Graphene Oxide by Nitrogen Doping. Chemistry – A European Journal, 20(38), 11999–12003. https://doi.org/10.1002/chem.201403833

Saska, S., Teixeira, L. N., Tambasco de Oliveira, P., Minarelli Gaspar, A. M., Lima Ribeiro, S. J., Messaddeq, Y., & Marchetto, R. (2012). Bacterial cellulose-collagen nanocomposite for bone tissue engineering. Journal of Materials Chemistry, 22(41), 22102. https://doi.org/10.1039/c2jm33762b

Shao, W., Liu, H., Liu, X., Wang, S., & Zhang, R. (2015). Anti-bacterial performances and biocompatibility of bacterial cellulose/graphene oxide composites. RSC Adv., 5(7), 4795–4803. https://doi.org/10.1039/C4RA13057J

Song, N., Hou, X., Chen, L., Cui, S., Shi, L., & Ding, P. (2017). A Green Plastic Constructed from Cellulose and Functionalized Graphene with High Thermal Conductivity. ACS Applied Materials & Interfaces, 9(21), 17914–17922. https://doi.org/10.1021/acsami.7b02675

Song, N., Jiao, D., Ding, P., Cui, S., Tang, S., & Shi, L. (2016). Anisotropic thermally conductive flexible films based on nanofibrillated cellulose and aligned graphene nanosheets. J. Mater. Chem. C, 4(2), 305–314. https://doi.org/10.1039/C5TC02194D

Tao, H., Yan, C., Robertson, A. W., Gao, Y., Ding, J., Zhang, Y., … Sun, Z. (2017). N-Doping of graphene oxide at low temperature for the oxygen reduction reaction. Chem. Commun., 53(5), 873–876. https://doi.org/10.1039/C6CC08776K

Vilela, C., Pinto, R. J. B., Pinto, S., Marques, P., Silvestre, A., & da Rocha Freire Barros, C. S. (2018). Polysaccharide Based Hybrid Materials. Cham: Springer International Publishing. https://doi.org/10.1007/978-3-030-00347-0

Wan, C., Jiao, Y., & Li, J. (2017). Flexible, highly conductive, and free-standing reduced graphene oxide/polypyrrole/cellulose hybrid papers for supercapacitor electrodes. J. Mater. Chem. A, 5(8), 3819–3831. https://doi.org/10.1039/C6TA04844G

Wan, C., & Li, J. (2016). Graphene oxide/cellulose aerogels nanocomposite: Preparation, pyrolysis, and application for electromagnetic interference shielding. Carbohydrate Polymers, 150, 172–179. https://doi.org/10.1016/j.carbpol.2016.05.051

Wang, L., Urbas, A. M., & Li, Q. (2018). Nature-Inspired Emerging Chiral Liquid Crystal Nanostructures: From Molecular Self-Assembly to DNA Mesophase and Nanocolloids. Advanced Materials, 0(0), 1801335. https://doi.org/10.1002/adma.201801335

Wei, H., Rodriguez, K., Renneckar, S., & Vikesland, P. J. (2014). Environmental science and engineering applications of nanocellulose-based nanocomposites. Environ. Sci.: Nano, 1(4), 302–316. https://doi.org/10.1039/C4EN00059E

Wei, X., Huang, T., Yang, J. hui, Zhang, N., Wang, Y., & Zhou, Z. wan. (2017). Green synthesis of hybrid graphene oxide/microcrystalline cellulose aerogels and their use as superabsorbents. Journal of Hazardous Materials, 335, 28–38. https://doi.org/10.1016/j.jhazmat.2017.04.030

Wei, X., Xue, F., Qi, X. dong, Yang, J. hui, Zhou, Z. wan, Yuan, Y. ping, & Wang, Y. (2019). Photo- and electro-responsive phase change materials based on highly anisotropic microcrystalline cellulose/graphene nanoplatelet structure. Applied Energy, 236(November 2018), 70–80. https://doi.org/10.1016/j.apenergy.2018.11.091

Wen, Y., Wu, M., Zhang, M., Li, C., & Shi, G. (2017). Topological Design of Ultrastrong and Highly Conductive Graphene Films. Advanced Materials, 29(41), 1702831. https://doi.org/10.1002/adma.201702831

Wicklein, B., Kocjan, A., Salazar-Alvarez, G., Carosio, F., Camino, G., Antonietti, M., & Bergström, L. (2014). Thermally insulating and fire-retardant lightweight anisotropic foams based on nanocellulose and graphene oxide. Nature Nanotechnology, 10(3), 277–283. https://doi.org/10.1038/nnano.2014.248

Wong, D. B., Sokolowsky, K. P., El-Barghouthi, M. I., Fenn, E. E., Giammanco, C. H., Sturlaugson, A. L., & Fayer, M. D. (2012). Water Dynamics in Water/DMSO Binary Mixtures. The Journal of Physical Chemistry B, 116(18), 5479–5490. https://doi.org/10.1021/jp301967e

Xiong, R., Kim, H. S., Zhang, L., Korolovych, V. F., Zhang, S., Yingling, Y. G., & Tsukruk, V. V. (2018). Wrapping Nanocellulose Nets around Graphene Oxide Sheets. Angewandte Chemie International Edition, 57(28), 8508–8513. https://doi.org/10.1002/anie.201803076

Yakout, A. A., El-Sokkary, R. H., Shreadah, M. A., & Abdel Hamid, O. G. (2017). Cross-linked graphene oxide sheets via modified extracted cellulose with high metal adsorption. Carbohydrate Polymers, 172, 20–27. https://doi.org/10.1016/j.carbpol.2017.05.004

Yang, W., Zhang, Y., Liu, T., Huang, R., Chai, S., Chen, F., & Fu, Q. (2017). Completely Green Approach for the Preparation of Strong and Highly Conductive Graphene Composite Film by Using Nanocellulose as Dispersing Agent and Mechanical Compression. ACS Sustainable Chemistry & Engineering, 5(10), 9102–9113. https://doi.org/10.1021/acssuschemeng.7b02012

Yao, Q., Fan, B., Xiong, Y., Jin, C., Sun, Q., & Sheng, C. (2017a). 3D assembly based on 2D structure of Cellulose Nanofibril/Graphene Oxide Hybrid Aerogel for Adsorptive Removal of Antibiotics in Water. Scientific Reports, 7(December 2016), 1–13. https://doi.org/10.1038/srep45914

Yao, Q., Fan, B., Xiong, Y., Jin, C., Sun, Q., & Sheng, C. (2017b). 3D assembly based on 2D structure of Cellulose Nanofibril/Graphene Oxide Hybrid Aerogel for Adsorptive Removal of Antibiotics in Water. Scientific Reports, 7(December 2016), 1–13. https://doi.org/10.1038/srep45914

Zhan, Y., Xiong, C., Yang, J., Shi, Z., & Yang, Q. (2019). Flexible cellulose nanofibril/pristine graphene nanocomposite films with high electrical conductivity. Composites Part A: Applied Science and Manufacturing, 119, 119–126. https://doi.org/10.1016/j.compositesa.2019.01.029

Zhang, X., Liu, P., Duan, Y., Jiang, M., & Zhang, J. (2017). Graphene/cellulose nanocrystals hybrid aerogel with tunable mechanical strength and hydrophilicity fabricated by ambient pressure drying technique. RSC Advances, 7(27), 16467–16473. https://doi.org/10.1039/C6RA28178H

Zhang, Y., Wang, F., Zhang, D., Chen, J., Zhu, H., Zhou, L., & Chen, Z. (2017). New type multifunction porous aerogels for supercapacitors and absorbents based on cellulose nanofibers and graphene. Materials Letters, 208, 73–76. https://doi.org/https://doi.org/10.1016/j.matlet.2017.04.141

Zheng, Q., Cai, Z., Ma, Z., & Gong, S. (2015). Cellulose Nanofibril/Reduced Graphene Oxide/Carbon Nanotube Hybrid Aerogels for Highly Flexible and All-Solid-State Supercapacitors. ACS Applied Materials & Interfaces, 7(5), 3263–3271. https://doi.org/10.1021/am507999s

Zhou, S., Zhou, L., Zhang, Y., Sun, J., Wen, J., & Yuan, Y. (2019). Upgrading earth-abundant biomass into three-dimensional carbon materials for energy and environmental applications. Journal of Materials Chemistry A, 7(9), 4217–4229. https://doi.org/10.1039/C8TA12159A
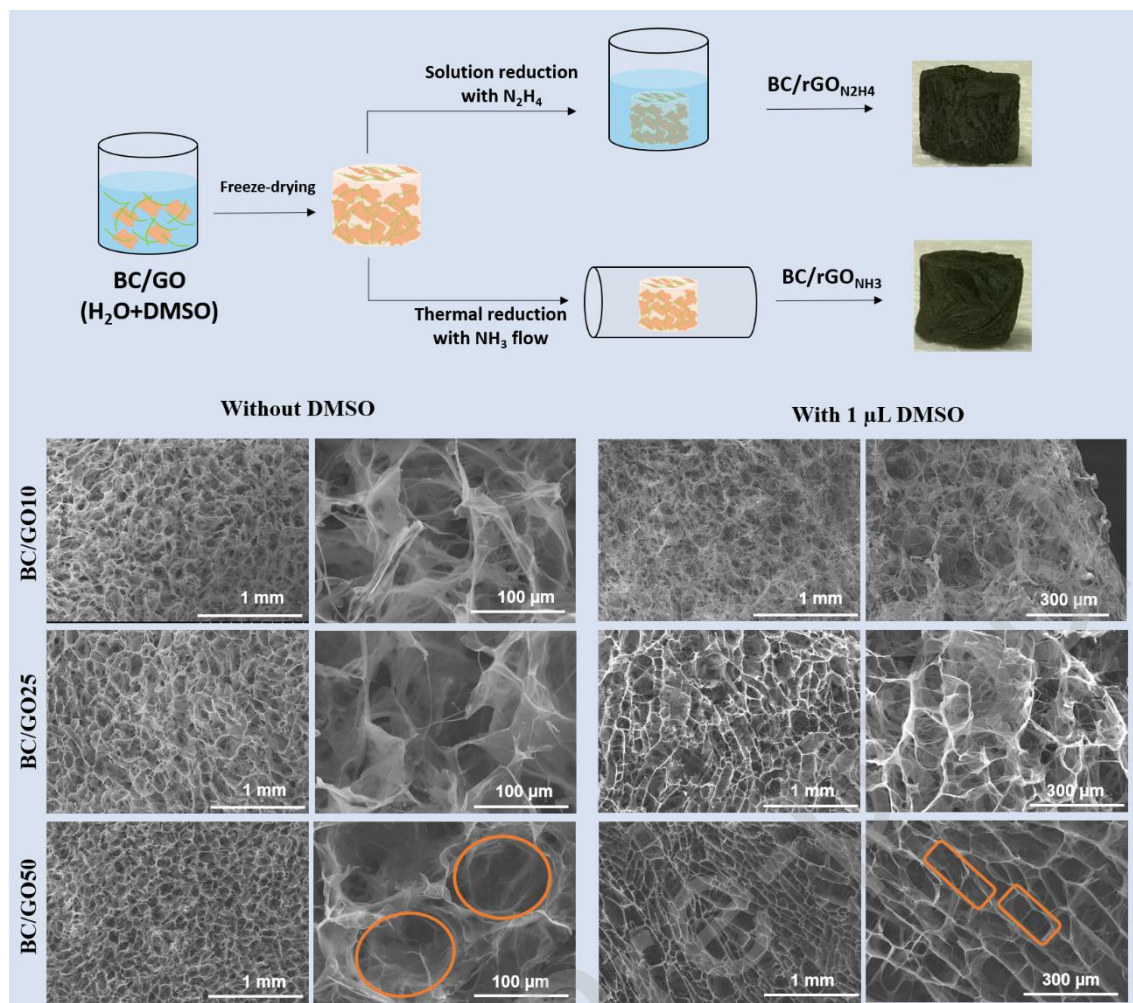
Figure 1. Schematic diagram of aerogels preparation and optical appearance. Comparison of the SEM images obtained at the cross-section of the different BC/GO aerogels, prepared with and without DMSO.
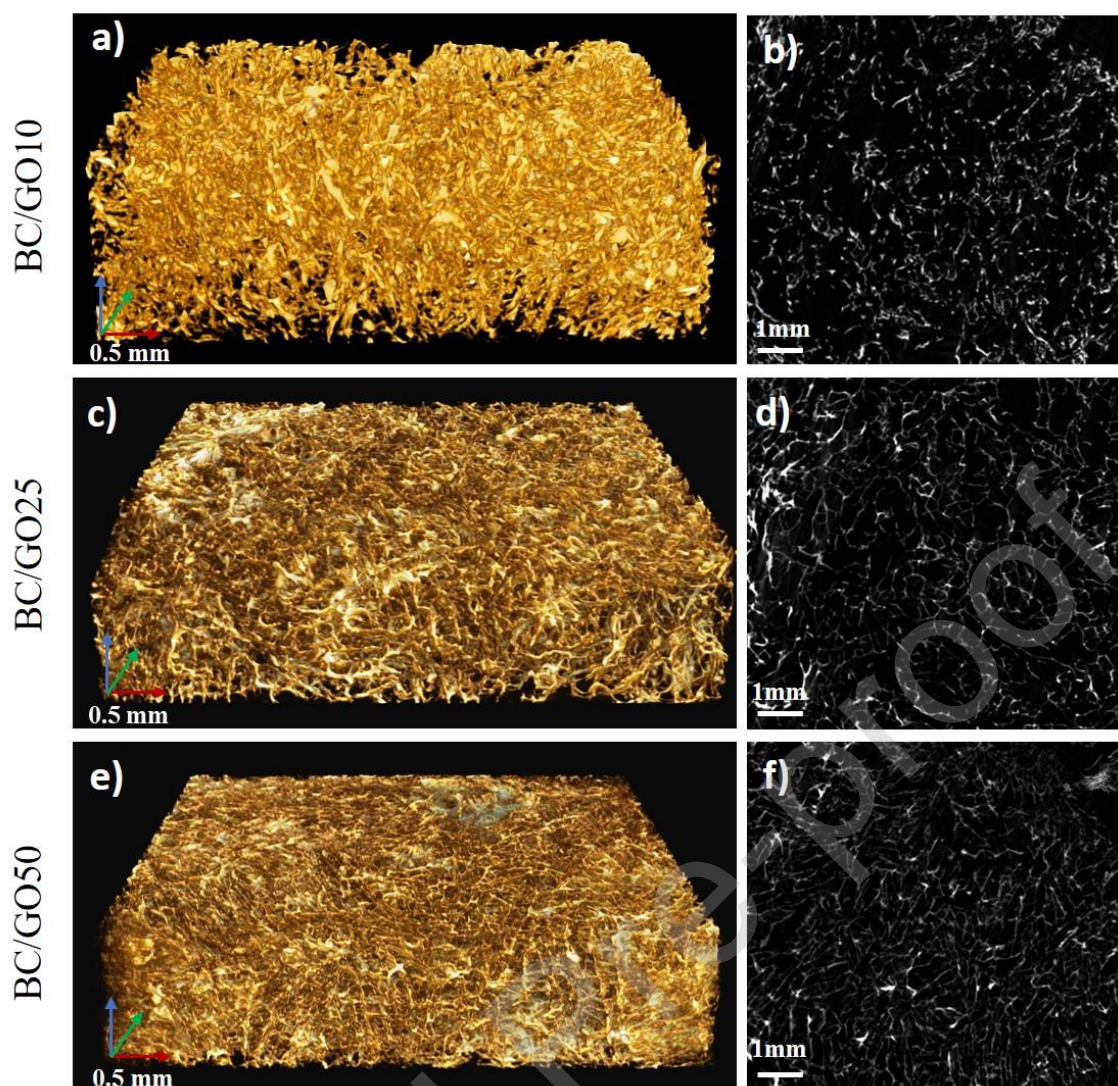
Figure 2. X-ray µtomography images of the BC/GO aerogels: 3D renderings of µCT images (BC/GO10 (a), BC/GO25 (c) and BC/GO50 (e) and segmented 2D slices (BC/GO10 (b), BC/GO25 (d) and BC/GO50 (f)).
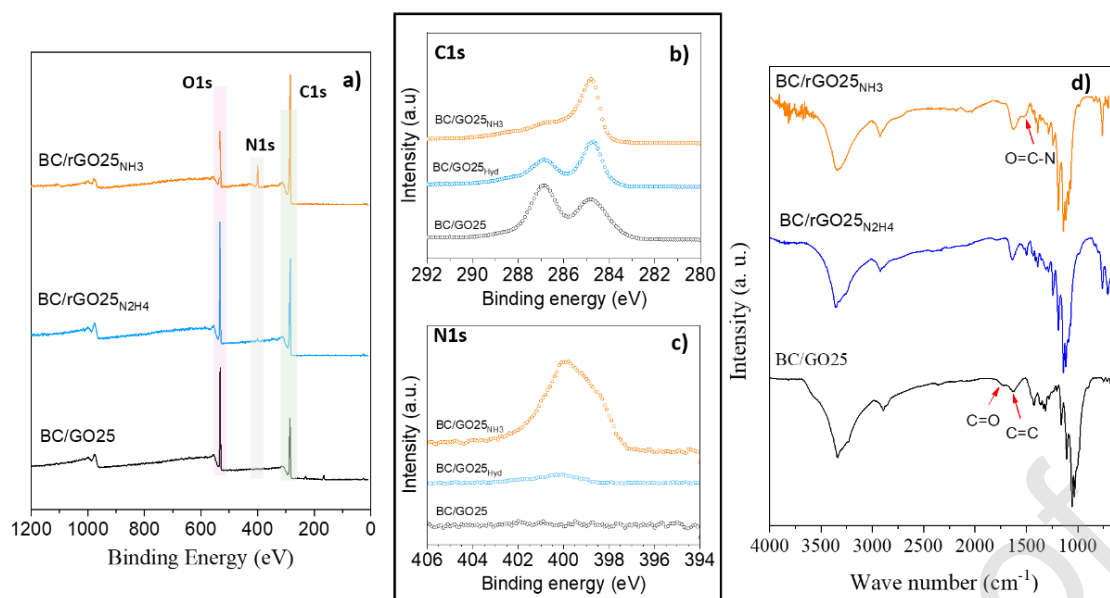
20

Figure 3. XPS spectra BC/GO25 and its reduced forms, XPS general survey scan (a) and high resolution C1s and N1s XPS spectra (b, c). FT-IR spectra (d).
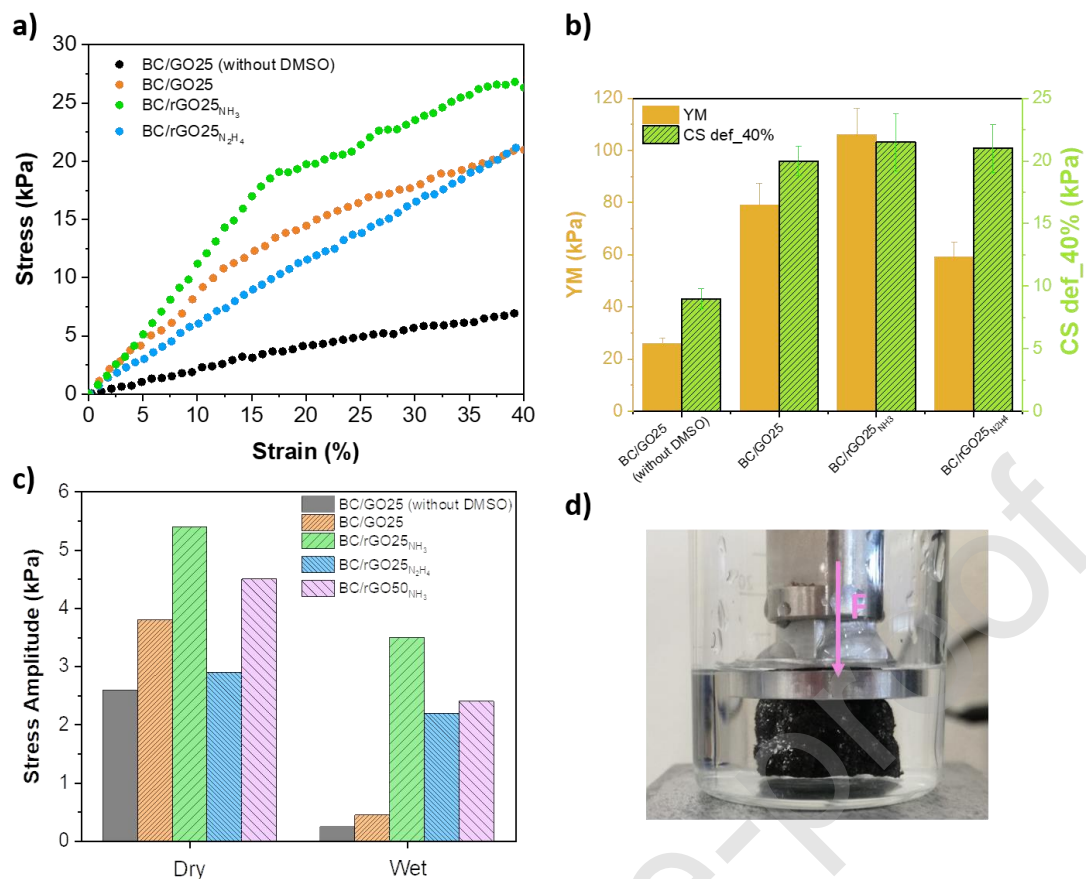
Figure 4. a) Stress-Strain curves for 40 % of strain, b) Young Modulus and compressive strength (CS) at 40 % of strain, c) Stress amplitude after 1,000 cycles of compression and d) Real image of the scaffolds under dynamic compression test in wet environment.
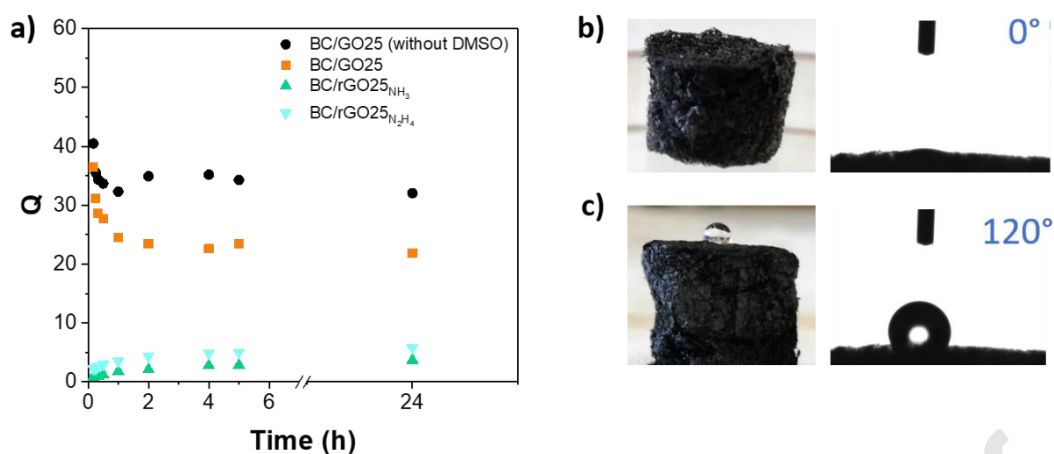
22

Figure 5. (a) Swelling ratio of the aerogels immersed in water as a function of time and water contact angles for aerogels reduced with (b) N2H4 and (c) NH3.
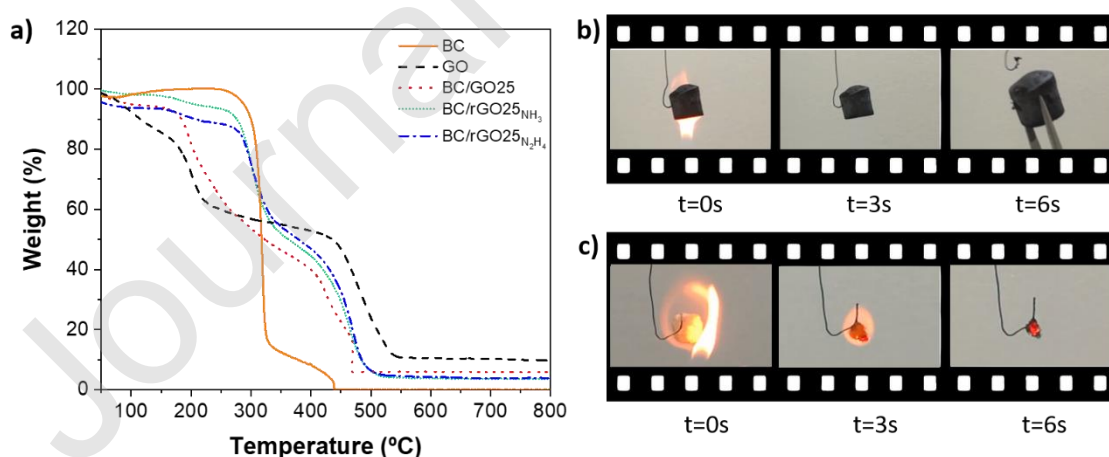

Figure 6. (a) Thermogravimetric analysis of BC, GO and BC/GO25 aerogels. Flame behaviour of (b) BC/rGO25NH3 and (c) BC specimens. Figure (b) the frames captured at t0 and t3s show the dimensional stability of the aerogel after flame exposure and frame t6s exhibit the ability to be handled without suffer collapse. Figure (c) the frame sequence (t0s, t3s and t6s) showed the continuous annealing degradation of the sample.

23

24

Table 1. C, O and N content of BC and BC/GO aerogels determined by XPS.

Sample	C (at. %)	O (at. %)	N (at. %)	Ratio O/C	Ratio N/C
BC/GO25	70.5	29.5	-	0.42	-
BC/rGO25N2H4	74.9	24.2	0.9	0.32	0.01
BC/rGO25NH3	77.8	13.9	8.3	0.18	0.11
BC/GO50	66.7	33.1	-	0.50	-
BC/rGO50N2H4	74.8	23.9	1.3	0,32	0.02
BC/rGO50NH3	81.7	17.2	1.1	0.21	0.01

Table 2. Electric conductivities for the different BC/GO aerogels.

Sample	Electric Conductivity (S/m)
BC/GO25	5.9×10^{-7}
BC/rGO25N2H4	1.7×10^{-3}
BC/rGO25NH3	7.2×10^{-1}
BC/rGO50NH3	8.7×10^{-1}